Thesis Title

Department of Physics, The University of Hong Kong, Pokfulam Road, Hong Kong

Wang Wenchao

3030053350

Contents

Abstract

Recent observations find that some millisecond pulsars (known as Class II MSPs) show aligned pulse profile es in different energy bands. Conventionally, radio and gamma-ray emission are produced in different regions—in polar cap and outer gap respectively. The finding of Class II MSPs implies that radio, X-ray and gamma-ray emission can all be emitted in outer gap. This means that Class II MSPs can have a different emission mechanism. Recently, scientists propose a model suggesting that hard X-ray can be emitted by inverse Compton scattering between radio waves and energetic charged particles. The objective of the thesis is to test this model by measuring hard X-ray spectra of some Class II MSPs using *NuSTAR*.

Chapter 1

Introduction

1.1 Neutron Stars and Pulsars

Neutron stars are produced by a supernova explosion of massive stars which have about 4 to 8 solar mass. After the supernova explosion, the star leaves a central region. And the central region collapses because of the effect of gravity until protons and electrons combine to form neutrons $(e^- + p \rightarrow n + \nu_e)$ —the reason why they are called "neutron stars". Because neutrons have no electromagnetic force on each other, they can be squeezed very tightly. Therefore, a neutron star has tremendous high density (about $5 \times 10^{17} kg/m^3$) and its diameter and mass is about 20km and 1.4 solar mass respectively. What prevents a neutron star to continue to contract is the degeneracy pressure of neutrons.

Pulsars are fast-spinning neutron stars. Their rotational periods can be from a few milliseconds to several seconds. For example, the rotational period of PSR B1937+21 is about $1.56ms$ while PSR B1919+21 is approximately $1.34s$. As we know, a star can be ripped by centrifugal force if the star rotates too fast. We can estimate lower limit of density of a star with the equation: $\rho = \frac{3\pi}{P^2 G}$, where P is the rotational period of a pulsar. Just for simplicity, we let P be $1s$. Then we get $\rho \approx 1.4 \times 10^{11} kg/m^3$. With the knowledge that the density of a white dwarf is about $1 \times 10^9 kg/m^3$ which is smaller than the lower density limit, the observed fast-spinning stars belong to the kind of stars which are much denser than white dwarf. As a result, neutron stars are ideal candidates for pulsars.

More than 2000 pulsars have been found so far. Most of them are in the disk of our Galaxy while we also can find a small portion of them in high latitude, which can be seen clearly in the figure 1.1. This may because they cannot escape the gravitational potential if their kinetic energy is not large enough. Besides, even though they have large enough velocities to escape from their birth region, there are some probabilities that they become nearly non-detectable before reaching high latitude.

<**add**>can add these content later.</**add**>

1.2 Emission Mechanism of Pulsars

Although emission mechanism of pulsars has not been fully understood yet, some models are developed trying to explain observational facts. The following is one toy model that
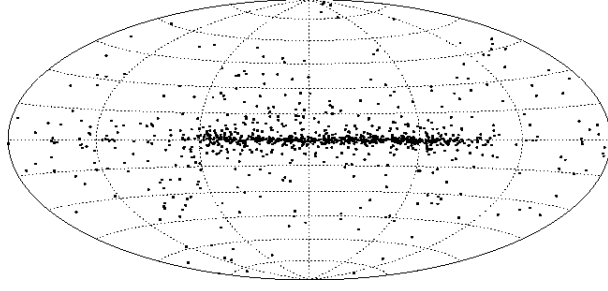
Figure 1.1: *Spatial distribution of some pulsars in galactic coordinate system.*

can explain some basic features of pulsars.

1.2.1 Magnetic Dipole Model

Assume a pulsar has a magnetic dipole moment $\vec{m}$, the angel between rotation axis and direction of $\vec{m}$ is α, its angular velocity is Ω, radius is R and moment of inertia is I. Also by assuming that energy of electromagnetic radiation are all from rotational energy, its spin-down rate can be written as:

$$\dot{\Omega} = -\frac{B_p^2 R^6 \Omega^3 \sin\alpha^3}{6c^3 I}$$

where B_p is magnetic field strength in the pole of the pulsar. Its surface magnetic field can also be estimated by:

$$B_s = \sqrt{\frac{3c^3 I}{2\pi^2 R^6} P\dot{P}} = 3.2 \times 10^{19}\sqrt{P\dot{P}}$$

where B_s is the strength of surface magnetic field.

In general, a pulsar's spin down rate can be expressed as: $\dot{\Omega} = -K\Omega^n$, where K is a constant and n is called braking index. In magnetic dipole model n is 3 (*H.Tong 2015*). Then characteristic age of the pulsar can be defined as: $P/2\dot{P}$ in magnetic dipole model. For example, the Crab pulsar's rotation period is about $0.033s$ and period derivative is $4.22 \times 10^{-13} s/s$. The characteristic age is about 1200 years. The pulsar is remnant of a supernova which is observed by ancient astronomers in 1054 AD, so the record shows that characteristic age can give us order of magnetic estimate of a pulsar's real age.

Although braking index is 3 in magnetic dipole model, most of pulsars' braking index is less than 3 as shown in figure 1.2. The reason is that if a pulsar's spin down is completely because of pulsar wind, the braking index is 1. Thus, the real braking index should be a combination of 1 and 3, which is usually less than 3 (*Oliver Hamil 2014*).

1.2.2 A More Sophisticated Model

It is oversimplified to regard a pulsar as a magnetized sphere rotating in vacuum. Actually, there are plenty of charged particles in a pulsar's magnetosphere which co-rotate with the pulsar. The creation of charged particles can be described by the following steps (*P.A.Sturrock 1971*).

1. The co-rotating charged primary particles emit gamma-ray by curvature radiation because of acceleration in super strong magnetic field.

Pulsar	n_{obs}	Ω	$\dot{\Omega}$
		s^{-1}	$10^{-10}s^{-2}$
PSR B0531+21 (Crab)	2.51±0.01	30.22543701	-3.862283
PSR B0540−69	2.14±0.01	19.8344965	-1.88383
PSR B0833−45 (Vela)	1.4±0.2	11.2	-0.157
PSR B1509−58	2.839±0.001	6.633598804	-0.675801754
PSR J1846−0258	2.16±0.13	3.0621185502	-0.6664350
PSR J1833−1034	1.857±0.001	16.159357	-0.5275017
PSR J1119−6127	2.684±0.001	2.4512027814	0.2415507
PSR J1734−3333	0.9±0.2	0.855182765	-0.0166702

Figure 1.2: *Braking index of some pulsars.*

2. In super intense magnetic field, the high energy photons decay into electrons and positrons which are called secondary particles by the process: $\gamma + (B) \rightarrow e^+ + e^- + (B)$. Synchrotron photons can be emitted by these secondary particles.

3. Secondary particles are also accelerated in strong magnetic field which is just like primary particles. As a result, these charged particles can create more secondary particles.

This chain of process is quite efficient to produce charged particles and pulsar's magnetosphere is filled with plasma as a consequence. So, it is natural to think of the distribution of charges in pulsar's magnetosphere. A characteristic charge density $\rho_{GJ} = -\frac{\vec{\Omega} \cdot \vec{B}}{2\pi c}$ is called Goldreich-Julian density. This charges can offset part of electric field ($E_{\parallel}$) which is parallel to magnetic field. There is some region in the magnetosphere called "outer gap" where ρ_{GJ} is so small that it can't screen $E_{\parallel}$ effectively. As a result, the secondary particles can be accelerated at a very large velocity (Lorentz factor $\gamma \sim 10^7$) and emit gamma-ray. Photons in outer gap can also create electrons and positrons by the process: $\gamma + \gamma \rightarrow e^- + e^+$. At the outer gap, one-photon pair production can't happen because magnetic field is too weak in this region.

1.3 Millisecond Pulsar

1.3.1 P-$\dot{P}$ Diagram

P-$\dot{P}$ diagram is an important tool for analyzing evolution of pulsars. Period (P) and time derivative of period ($\dot{P}$) are two of pulsars' important characteristics. Analyzing the position of a pulsar in P-$\dot{P}$ diagram can give some valuable information such as which evolution stage the pulsar is in or the type of the pulsar, etc. The figure 1.3 is an example of P-$\dot{P}$ diagram. The horizontal axis is pulsars' rotation periods and the vertical axis is time derivative of rotation periods. In this P-$\dot{P}$ diagram, the negative slope lines represent the strength of surface magnetic field while the positive slope lines represent the characteristic age of pulsars. The following is a short explanation for this. From previous discussion, we have known that the characteristic age of a pulsar is $\tau = -P/\dot{P} = P/(-\dot{P})$, so line of constant τ is a set of straight lines with equal positive slope. We also know $B \propto \sqrt{P\dot{P}}$, therefore the line of constant B should be a part of hyperbola. When $\dot{P}$ is very small, the hyperbola looks like a straight line with negative slope.
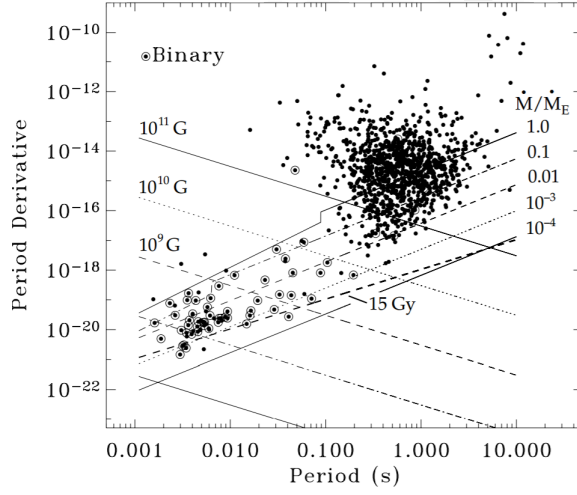
Figure 1.3: *Position of pulsars in P-$\dot{P}$ diagram*

This figure shows that most pulsars lie in the position about $1s, 10^{-14}s/s$. At the same time, a couple of stars lie at the bottom-left of the figure—these are millisecond pulsars (MSP). Their rotation periods are about 1-20 milliseconds. It is believed that MSPs are spun up by accretion of mass from its companion star. In the above P-$\dot{P}$ diagram, we can observe that millisecond pulsars' surface magnetic field are about 3 to 4 orders of magnitude lower than those of normal pulsars. However, an MSP has a relative strong magnetic field near its light cylinder. The reason is that an MSP's radius of light cylinder ($R_{lc} = c/\omega$) is much smaller than a normal pulsar's because of its short rotation period and the magnetic field near light cylinder can be estimated as $B_{lc} \sim (R/R_{lc})^3$. At the same time, pulsars' emission mechanism is closely related to their magnetic field near light cylinder. As a result, like a normal pulsar, an MSP also have broadband spectrum from radio to gamma rays.

1.3.2 Origin Of Millisecond Pulsars

From pulsars' emission mechanism, we know that magnetic field of a pulsar decreases with time while the spin period increase with time. But MSPs' spin period is much shorter than normal pulsars and surface magnetic field is a lot weaker. This makes an MSP seem to be both young and old. As a result, people think millisecond pulsars are old pulsars spun up by its companion. The companion star transfer mass and angular momentum to accelerate the pulsar. Therefore, the aged pulsar can spin faster gradually.

Mass Transfer And Accretion In Binary Systems

X-ray binaries are a type of binary systems that is luminous in X-ray band. There are several kinds of X-ray binaries including low mass X-ray binaries (LMXB) and high mass X-ray binaries (HMXB). The way of transferring mass is different in these two types of systems. Before discussing mass transfer, we need to know a little bit about Roche Lobe. The figure 1.4 is a schematic diagram of Roche lobe.

We call two stars in an LMXB as A and B respectively for convenience. It is obvious that if an object is close to star A, the gravitational influence of A is so strong that we can nearly ignore the effect of star B. Similarly, this is true for star B. As a result, there
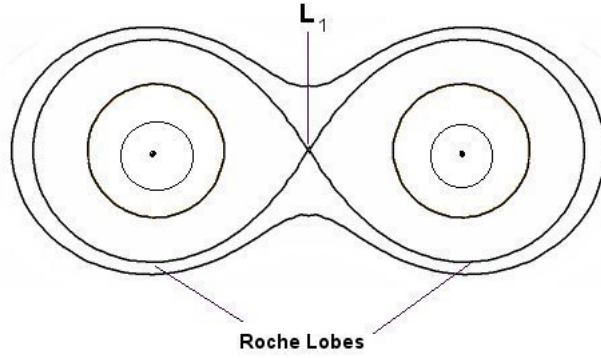
Figure 1.4: *Schematic diagram of Roche lobe.* L_1 is called inner Lagrange point which is the intersection of equipotential lines of star A and B.

must be a point where the effect of star A is equal to star B which is called inner Lagrange point (*Seidov 2013*). The two volumes inside the largest equipotential lines of A and B are called Roche lobe. If star B cross its Roche lobe, than its mass will be attracted by A thus mass transfer between A and B happens. We should notice that this is the main way of mass transfer in LMXB. While in HMXB, the mass can be transferred by strong wind of the massive companion star.

What should be noted is that mass transfer can change the distance between two companion stars. If low-mass star transfer mass to high-mass companion star, the orbital separation will be large. This can actually stop mass transfer and is like negative feedback. On the contrary, mass transfer from high-mass star to low-mass star will shrink the orbital distance.

1.3.3   Class II MSPs
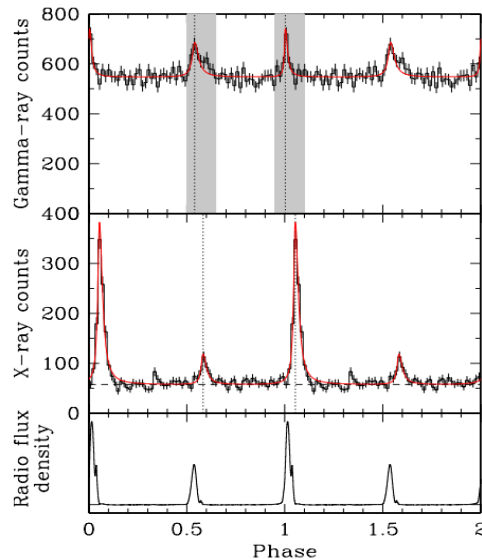
Figure 1.5: *Pulse profiles of PSRJ1939+2134 in radio, X-ray and gamma-ray.*

Radio emission are usually considered to be emitted above the polar cap, which means radio emission and gamma-ray emission are from different location of pulsar's magneto-sphere. However, there are about 10 sources showing aligned pulse profiles in radio and

gamma-ray implying that radio emission may produced from outer magnetosphere and they are called Class II MSPs (*Guillemot et al. 2012*). These pulsars have strong magnetic field near the light cylinder. The figure 1.5 is an example of aligned pulse profile.

1.4 Objectives

Recently, it is found that X-ray band of spectrum of millisecond pulsar B1937+21 has a hard photon index of 0.9±0.1 by analyzing data of *Chandra, XMM-Newton Fermi* (*Ng et al. 2014*). People think X-ray emission is mainly produced by synchrotron radiation, but it is difficult to explain such a hard photon index. Besides millisecond pulsar B1937+21, it is discovered that hard photon index is a common characteristic of class II MSPs. Therefore, people propose that Inverse Compton scattering can also lead to X-ray emission and build a model recently to explain it (*Ng et al. 2014*).

In order to test the model, we need to analyze the hard X-ray band of millisecond pulsars B1937+21, J0218+4232 and B1821-24. The energy ranges of *Chandra* and *XMM-Newton* are up to 10keV and 15keV respectively while *NuSTAR* can be up to 79keV. As a result, we aim to use *NuSTAR* to measure the hard X-ray band of the three MSPs mentioned above.

Chapter 2

Gamma-Ray Analysis

As mentioned before, because of the very short rotation periods, MSPs have very small light cylinder radii compared with normal pulsars. As a result, their emission mechanisms are similar to normal pulsars, especially for my target objects — PSRJ0218+4232, PSRJ1939+2134 and PSRJ1824-2452 which are among the fastest spinning MSPs. Therefore, as normal pulsars, these three pulsars are bright in Gamma-Ray band so it is convenient for us to analyze the spectra properties of them in gamma-rays.

2.1 Gamma-Ray Emission Mechanism of MSPs

An MSP's magnetosphere is dominated by various kinds of emission mechanisms. Thus we should review some fundamental emission mechanism firstly, including synchrotron radiation, curvature radiation and inverse-Compton radiation.

2.1.1 synchrotron radiation

Synchrotron radiation is a special case of cyclotron radiation when particles' speed is comparable to the speed of light. Because of the relativistic beaming effect, we will observe a very short radiation pulse when speed of particles is large. We only aim to analyze the spectrum properties of MSPs, so we focus on the spectrum property of synchrotron radiation. The power spectrum of a single electron can be described by the function 2.1

$$P\left(\nu\right) = \frac{\sqrt{3}e^3 B \sin\alpha}{mc^2} \left(\frac{\nu}{\nu_c}\right) \int_{\nu/\nu_c}^{\infty} K_{5/3}\left(\eta\right) d\eta \tag{2.1}$$

where ν_c is the critical frequency and $K_{5/3}$ is modified Bessel function. The critical frequency can be expressed by the function 2.2

$$\nu_c = \frac{3}{2}\gamma^2 \nu_{cyc} \sin\alpha \tag{2.2}$$

where α is the pitch angle and the ν_{cyc} is the frequency of corresponding cyclotron radiation.

These function does not give us very much information because of the integration of the modified Bessel function. We let $x = \nu/\nu_c$ and fix the environment variables such as magnetic field (B), the function 2.1 becomes:

$$P(\nu) = C \times x \int_x^\infty K_{5/3}(\eta)\, d\eta \tag{2.3}$$

where C is a constant dependent on B. Thus, in order to analyze the power spectrum of synchrotron radiation, we only concentrate on the later part, which is

$$F(x) = x \int_x^\infty K_{5/3}(\eta)\, d\eta \tag{2.4}$$
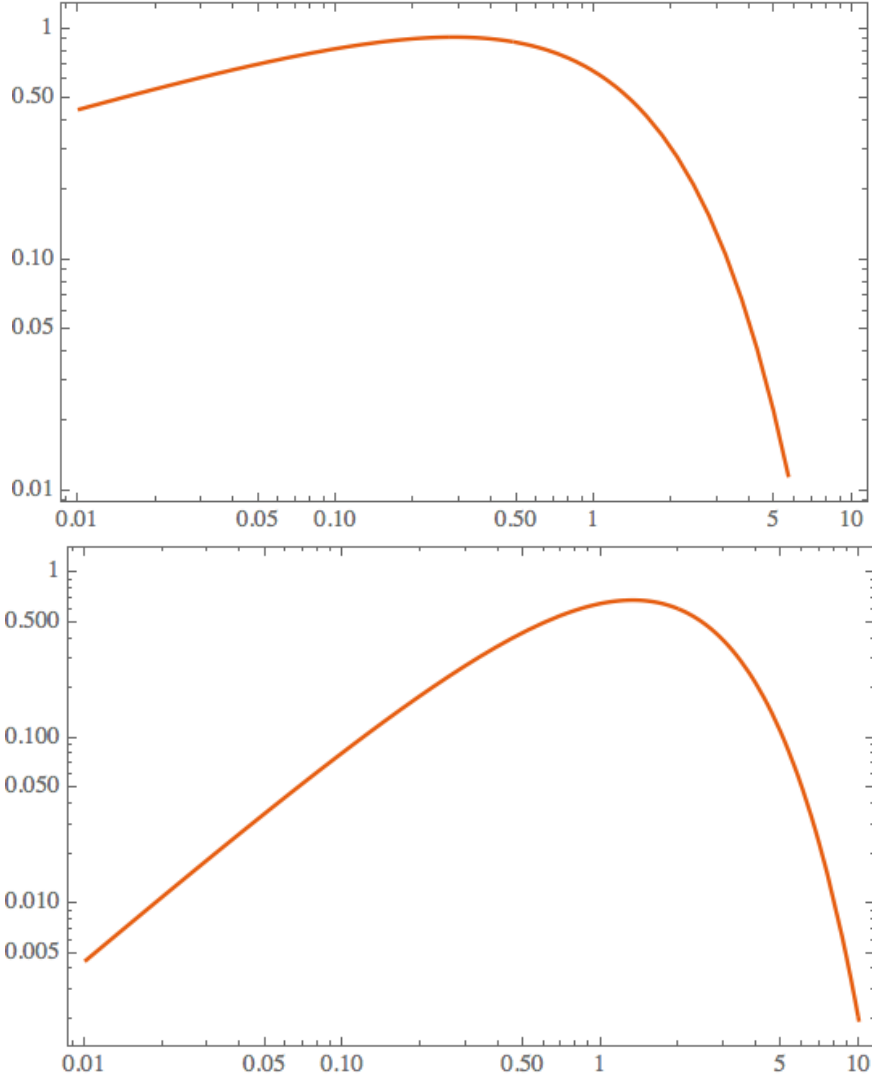
Figure 2.1: *According to the function 2.4, top: $F(x)$; bottom: $xF(x)$.* <*change*>*should change the style of the figure.*</*change*>

The top figure 2.4 describes the general shape of power spectrum of synchrotron radiation When the frequency is larger than the critical frequency ν_c, the power goes down dramatically. However, the top figure does not show the information that at what frequency the electron emit the strongest power, which is in the bottom figure. The bottom figure shows that the energy most energy emitted around critical frequency.

In reality, synchrotron radiations are not generated by a single particle. We describe the number density distribution of electrons with respect to energy by a single power-law model as the function 2.5 shown.

$$N(E) \approx CE^{-\delta} \tag{2.5}$$

For simplicity, we set the ambient magnetic field B to be a constant and make an approximation that all radiations are at a single frequency:

$$\nu \approx \gamma^2 \nu_{cyc} \tag{2.6}$$

where the meaning of ν_{cyc} is the same as function 2.2. Our objective is to know the relationship between total power of all electrons and their radiation frequency. We describe the relationship as the function 2.7

$$-P(E) N(E) dE = Q_\nu d\nu \tag{2.7}$$

$$P(E) = \frac{4}{3}\sigma_T \beta^2 \gamma^2 c U_B \tag{2.8}$$

where σ_T is electron Thompson scattering section, U_B is energy density of the environment magnetic field, Q_{nu} is the emission coefficient of synchrotron radiation and $E = \gamma m_e c^2$. With function 2.6, we have

$$P = \frac{dE}{d\nu} = \frac{m_e c^2}{2\sqrt{\nu \nu_{cyc}}} \tag{2.9}$$

Combine the function 2.9 and 2.7 we get:

$$Q_\nu = \frac{4}{3}\sigma_T \beta^2 \gamma^2 c U_B \frac{m_e c^2}{2\sqrt{\nu \nu_{cyc}}} N(E) \tag{2.10}$$

By ignoring constants in the function 2.7 we have

$$Q_\nu \propto \nu^{(1-\delta)/2} \tag{2.11}$$

The function 2.11 shows that if the number density electrons is a power-law distribution, the spectrum of synchrotron radiation is also a power-lay model.

2.1.2 Inverse-Compton radiation

If a energetic relativistic photon collides with a charged particle from an proper incident angle, the photon's energy decreases and direction changes. This is a process of Compton Scattering. Inverse-Compton radiation is the opposite process by which a low energy photon gained energy from an ultra-relativistic electron.

As the figure 2.2 showing, in the laboratory frame (S), the incident angle and energy of a photon is θ and $h\nu$ respectively. The speed of the electron is v. In the electron rest frame (S'), we change the denotation to θ', $h\nu'$ and. Also, let the position of the electron be the origin point of S'. We can study the whole process in the S' frame, the transfer the result to the S frame by Lorentz transformation.
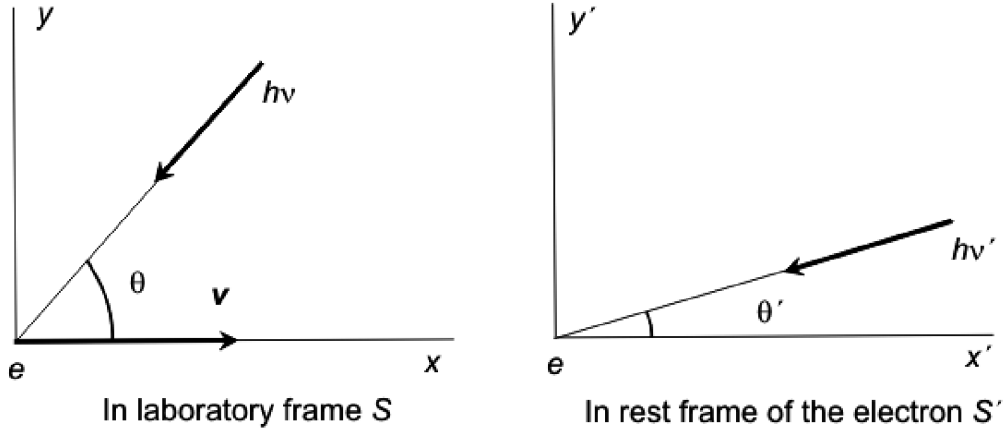
Figure 2.2: *Inverse Compton Diagram* <***Notice***>*this figure is from internet*</***Notice***>

In the S' frame, the electron is at rest so its energy is $m_e c^2$. For Inverse Compton scattering, the energy of an incident photon (less than several keV) is much less than the rest energy of an electron (about $0.51 MeV$) and the relationship can be expressed by $h\nu' \ll m_e c^2$. Therefore, this can be treated as Thompson Scattering process. Let the Poynting vector of incident photons be $\vec{S'}$ and their energy density be U'_{rad}, we have equation 2.12

$$\vec{S'} = c U'_{rad} \tag{2.12}$$

The electron absorbs the energy of the incident photons and then be accelerated. Thus the accelerated electron will emit part of energy taken from incoming photons and the power of scattered radiation is denoted as P'. The ratio can be described by Thompson Scattering cross section σ_T which is:

$$\sigma_T = \frac{8\pi}{3} \left(\frac{e^2}{m_e c^2} \right)^2 \tag{2.13}$$

and the relationship between the electron radiation power and incoming photon energy flux can be described by the equation 2.14

$$P' = \left| \vec{S'} \right| \sigma_T \tag{2.14}$$

Combine the equation 2.12 and 2.14, the radiation power emitted by the electron is:

$$P' = c \sigma_T U'_{rad} \tag{2.15}$$

Then we need to find the relationship between frame S and S'. It mainly contains 2 parts: the relationship between P, P' and U_{rad}, U'_{rad}. Since $P = dE/dt$ and dE/dt (<**question**>check</**question**>) is Lorentz invariant in inertial frame, we know:

$$P = P' \tag{2.16}$$

Now we hope to write U'_{rad} in terms of U_{rad}. U_{rad} is comprised by energy of a single photon and photon density. In the flowing analysis, all the denotations are correspondent to 2.2 According to the relativistic Doppler shift formula, we have:

$$h\nu' = (h\nu)\gamma(1 + \beta\cos\theta) \tag{2.17}$$

10

where $\beta = v/c$ and γ is Lorentz factor of an ultra-relativistic electron. Then we calculate the photon density. In the frame S', the photon density is inverse proportional to the time interval (Δt) between 2 photon strike the electron since total number of photons is Lorentz invariant. In laboratory frame S, we consider 2 photons collide with the electron at the 4-dimension vector of $(x_1, 0, 0, t_1)$ and $(x_2, 0, 0, t_2)$. According to the Lorentz transformation between inertial frames:

$$\begin{cases} x = \gamma \left(x' + \beta c t' \right) \\ y = y' \\ z = z' \\ t = \gamma \left(t' + \frac{\beta x'}{c} \right) \end{cases} \tag{2.18}$$

And since we set $x' = 0$, from equation 2.18, the 2 events of 2 successive photons collide with the electron can be expressed as: $(\gamma v t'_1, 0, 0, \gamma t'_1)$ and $(\gamma v t'_2, 0, 0, \gamma t'_2)$. As the Fig 2.3 showing, the time interval of two successive photons (reciprocal of frequency) in frame S is:

$$\begin{aligned} \Delta t &= (t_2 - t_1) + \frac{(x_2 - x_1) \cos \theta}{c} \\ &= \gamma (t'_2 - t'_1) + \frac{\gamma v (t'_2 - t'_1) \cos \theta}{c} \\ &= \Delta t' \gamma (1 + \beta \cos \theta) \end{aligned} \tag{2.19}$$

The equation 2.19 shows that the relationship of photon number density between frame S and S' is:

$$n' = n\gamma (1 + \beta \cos \theta) \tag{2.20}$$

Combine the equation 2.20 and 2.17 we can transfer the incident photon energy density from frame S to S' according to the equation 2.21

$$U'_{rad} = U_{rad} \left[\gamma (1 + \beta \cos \theta) \right]^2 \tag{2.21}$$

In the equation 2.21, the incoming photon energy density is a function of incident angle (θ), in order to get the total photon energy density, we integrate the equation over θ. Then we get:

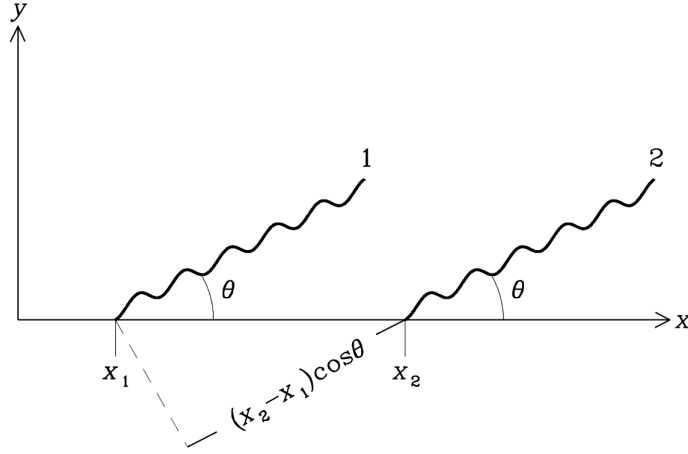$$U'_{rad} = \frac{4}{3} U_{rad} \left(\gamma^2 - \frac{1}{4} \right) \tag{2.22}$$

By combining the equation 2.22 and 2.15 we know the total scattered radiation power is:

$$\begin{aligned} P' &= P \\ &= \frac{4}{3} \sigma_T c U_{rad} \left(\gamma^2 - \frac{1}{4} \right) \end{aligned} \tag{2.23}$$

<add>inverse-compoton radiation</add>

2.1.3 Two-layer Model

After we have reviewed gamma-ray fundamental emission mechanism, we can proceed to the Two-layer model on which this thesis is mainly based. Two-layer model is a variation

Figure 2.3: *Two photons collide with an electron. In the frame S', two photons collide with a rest electron successively. In the frame S, the electron is no longer at rest and the positions of the two events are x_1 and x_2 <**Notice**>the figure is from internet</**Notice**>*

of outer-gap model since they both claim that the gamma-ray emission zone is close to the light-cylinder. However, in two-layer model, the outer layer consists of two regions — a primary acceleration region and a screening region.

In the primary region, charged particles moved out of pulsars along the open field lines, so the charge density is usually very low. However, by pair-production processes, a lot of e^- and e^+ are produced. But in the primary region where lots of pairs are created, the charge density doesn't change very much because the pairs have not been separated yet. With the help of strong electric field, the particles of different signs move to opposite directions. As a result, the two-layer model states that just above the primary region, a screening region will be created and the charge density is very large. This is basically the reason why there are two regions in pulsars' outer magnetosphere.

Then the next issue is that how we describe the distribution of charge density in these two regions. For simplicity, we just use a step function to represent the charge density distribution and step function can clearly shows the gap between the two regions. We use a magnetic dipole model to approximate the magnetic distribution in the magnetosphere. Since in magnetic dipole model, magnetic field at one position is only dependent on the position's distance from the source and altitude, we can also ignore the azimuthal distribution of charge density in our model and use the two parameters the $r(distance)$ and $\theta(altitude)$ to calculate the magnetic field at some position.

In the two-layer model, we can use three parameters to express the structure of a pulsar's outer magnetosphere - charge density of the primary region, the total length of the primary region and the screening region and the last one is the ratio of the thickness of the primary region and the screening region. The figure 2.4 shows the basic structure of two-layer model.

As the figure 2.4 showing, let the charge density of the primary region be $\rho_1 = (1-g_1)\rho_{GJ}$ and the total gap size is h_2, where ρ_{GJ} is Goldreich-Julian charge density. For convenience, we also denote the gap size of the primary region as h_1.
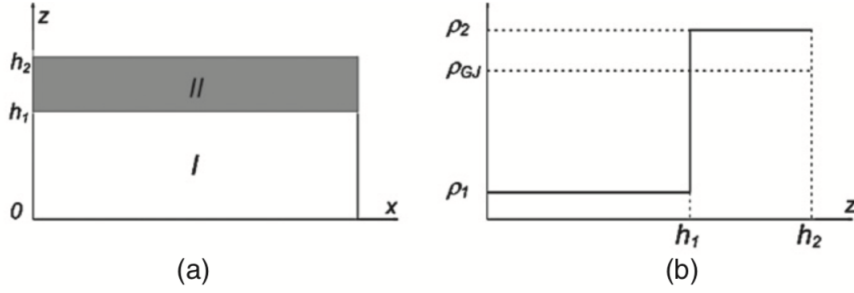
Figure 2.4: *(a): The geometry of two-layer model. h_1 and h_2 is the height of the primary region and the screening region respectively. (b): the charge densities of primary region and screening region. In the primary region, the charge density is much smaller than Goldreich-Julian charge density while is larger in the screening region. <**mayChange**>this figure is from the previous paper, I may need to regenerate the figure.</**mayChange**>*

We denote the electrical potential to be ϕ_0 which satisfies

$$\nabla^2 \phi_0 = -4\pi \rho_{GJ} \tag{2.24}$$

and the total electrical potential is $\phi = \phi_0 + \phi'$, where ϕ' is a representation of the deviation of the co-rotating electrical potential. Let total charge density is ρ and subtract the equation 2.24 we have

$$\nabla^2 \phi' = -4\pi \left(\rho - \rho_{GJ} \right) \tag{2.25}$$

Because the model has ignored the distribution in the azimuthal direction, we can use two parameters x, z to represent a position, where x is the direction along the magnetic field line and z is the perpendicular to the magnetic field line. In order to solve the equation 2.25, the model also makes 2 approximations. The first is that the directive of electrical potential ϕ is ignored. The second is that the Goldreich-Julian charge density is uniformly distributed along the magnetic line direction (x direction). These 2 approximations are based on the a reasonable assumption that the change rate for both electrical potential (ϕ') and Goldreich-Julian charge density (ρ_{GJ}) along the x direction is much smaller compared with z direction. As a result, the equation 2.25 can be written as:

$$\frac{\partial^2}{\partial z^2} \phi' = -4\pi \left(\rho - \rho_{GJ} \right) \tag{2.26}$$

In order to solve the equation 2.26, we have to have proper boundary conditions. First of all, we have to decide the boundary positions, which is determined by 4 parameters and they are $x_{lo}, x_{hi}, z_{lo}, z_{hi}$. It is reasonable to set x_{lo} and x_{hi} be the pulsar's surface and the light cylinder respectively and z_{lo} (lower boundary) be the last open field line. And let the electrical potential be 0 along the last open field line (this is because we have ignored the variation of electric field in x direction).

$$\phi \left(x, z_{lo} \right) = 0 \tag{2.27}$$

The position of z_{hi} is a little bit tricky. In order to make the electrical potential be continuous at $z = z_{hi} = h_2$, the model sets the $\phi' = 0$ since the non-corotating electrical potential outside the upper bound is 0 and the co-rotating potential is continuous near the boundary.

With these boundary conditions and equation 2.26, we can calculate the distribution of electric field, which accelerates charged particles to a very high speed so that they can emit curvature radiation, giving gamma-ray spectra. With the accelerating electric field known, we can calculate the Lorentz factor of charged particles and their spectra. This is the basic idea of the Two-layer model. <question>not sure if I should introduce the theory more thoroughly</question> .

<question>I am not sure if I should add this part here, since it is completely based on my own experience</question>

Constraints of The Two-lay Model Used In The Thesis

The simplified two-layer model is consistent with observation data to some extent. (The relevant data can be found in the paper *GAMMA-RAY SPECTRAL PROPERTIES OF MATURE PULSARS: A TWO-LAYER MODEL.*) The model uses 4 parameters to get a fair good prediction of gamma-ray spectra for many pulsars. And all these 4 parameters have a very obvious physical meaning. However, we can clearly find the "defects" of the model — it is somewhat oversimplified. Though there are other more sophisticated version of two-layer model, we use the simpler one, which may cause some inconsistency between our simulation and observation.

Therefore, we can briefly analyze which part is oversimplified and can be improved. First of all, we directly use a step function to describe the charged particle distribution. Though the charge density of the screening region is much larger than the primary region, using a step function is non-physical and may exaggerate the change rate of charge density. At the same time, the dramatic change of charge density also brings introduces some instability for numerical simulation.

Secondly, the model sets the total of screening region and primary region to be rectangular shape. Though the shape is not clear, it should not be a rectangular in theory and may be very different. In numerical simulation, changes in shape of the regions will directly lead to a different integration region, which may change the simulated spectra completely.

Thirdly, there are some inconsistency in the model itself according to the its assumption. For example, the model states that (for simplicity) the energy of charged particles accelerated in the primary region has been completely transferred to a photon-pairs by the pair creation process. It can be expressed as a function:

$$eE_{\parallel}c = l_{cur} \tag{2.28}$$

where $E_{\parallel}$ is the electric field strength along the magnetic field line and

$$l_{cur} = \frac{2e^2 c \gamma_e^4}{3s^2} \tag{2.29}$$

is the power of curvature radiation, where s is the radius of curvature. Combining the equation 2.28 and 2.29 we have:

$$\gamma_e = \left(\frac{3s^2}{2e} E_{\parallel} \right)^{1/4} \tag{2.30}$$

Since $E_{\parallel}$ can be 0, from the equation 2.29 we know that γ_e can also be 0, which is absolutely impossible. Although this may not have a big influence on the spectra, it is the problem that we should solve.

All in all, the model is simple and the gamma-ray spectra computed based on the model is consistent with observation data. There are many much more sophisticated two-layer model which are generalizations of model used in the thesis. Those models may have addressed the problems described above, but the model used in the thesis do have some defects.

<**mayAdd**>continue from here</**mayAdd**>

2.2 Introduction of The Fermi Gamma-ray Space Telescope

The Fermi Gamma-ray Space Telescope was launched on June 11, 2008 and opened a new window of studying supermassive black-hole systems, pulsars and so on. Its original name was Gamma-ray Large Area Space Telescope (GLAST) and changed to Fermi Gamma-ray Space Telescope in honor of a great scientist Enrico Fermi.

The Fermi Gamma-ray Space Telescope contains two parts: Gamma-ray Burst Monitor (GBM) and Large Area Telescope (LAT), which is the primary components and is at least 30 times more sensitive than all gamma-ray telescopes launched before. We only use LAT for our purposes. So we focus on the LAT instrument, which contains four main subcomponents including tracker, calorimeter, anti-coincidence detector and data acquisition system. The reason why the telescope is designed in this way is that high-energy gamma-rays cannot be refracted by lens or mirrors. As a result, the way that the Fermi LAT operates is totally different.
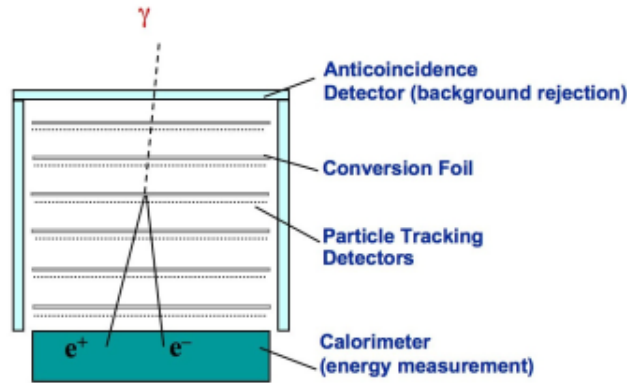
Figure 2.5: *Light curve of module A*

The following figure 2.5 demonstrates the very basic idea of the Fermi LAT working principles.

- Gamma-ray photons can enter the anti-coincidence detector freely while cosmic-rays will generate signals which can tell the data acquisition system to reject these particles. In this way, the Fermi LAT can distinguish the gamma-ray photons and high energy cosmic rays and the confidence is over 99.9%.

- The conversion foil (shown in the figure 2.5) can convert the gamma-ray photons into electron and positron pairs. This procedure makes it possible to determine the directions of the coming gamma-ray photons.

- The tracker (particle tracking detectors in the figure 2.5) records the positions of the electrons and positrons generated from the gamma-ray photons. There are many trackers so the paths of a particle can be constructed.

- The electrons and positrons reach the calorimeter hence their energies are also measured. Therefore, the energies of the original gamma-ray photons can also be calculated.

- The data acquisition system rejects unwanted particles such as cosmic rays by the method we mentioned before. Also, photons come from the Earth's astronomers are also rejected.

For a telescope, the ability of measuring the light direction and energy is very crucial. From the above descriptions of the Fermi LAT working principles, we know that the preciseness of construction of particles' path heavily influences how good we can measure the direction of photons. And this process is greatly dependent on algorithms, which means that with the improvements of software, the sensitivity of the telescope can also be improved. The Pass 8 data was released on June 24, 2015. It is an reprocessing of the entire Fermi mission dataset with better energy measurements, larger effective area, wider energy range and so on. This is part of the reason why I will redo the analysis of the three MSPs.

2.3 Analysis With Fermi LAT

In this section, my main objective is to show the results of my analysis. Before doing so, it is appropriate to briefly introduce some terminologies.

- The first is count maps. A count map is basically generated by the following steps. Firstly we choose a pixel with a certain size. Then we check each photon's direction to determine if the photon is in this pixel. If it is in the pixel, the photon counts of the pixel will add one. So more photons fall within the pixel, the more photon counts the pixel has, hence the brighter the pixel is. By doing the same thing for every pixel, a count map is generated. A count map let us know what we have observed intuitively and gives us a very basic idea of if we get the wanted data.

- A count cube is very similar to a count map, except that a count cube is divided in many energy bands. For example, a dataset whose energy is from 100MeV to 100GeV can be divided into 30 bins. We can generate a count map in each energy bin, so we have 30 count maps. In other words, we can regard a count cube as multiple count maps. A count cube's advantage over a count map is that we can observe distribution of gamma-ray photons in different energy range.

- TS value provides us a way to test if our target source is observed. The TS value is: $TS = -2\frac{\ln L_{max,0}}{\ln L_{max,1}}$, where $\ln L_{max,0}$ is the maximum likelihood value without the target source while $\ln L_{max,0}$ is the maximum likelihood value with the target

source. According to the equation, the smaller the ratio of $\ln L_{max,0}$ and $\ln L_{max,1}$, the larger the TS value is. Therefore, a larger TS value statistically means that our aimed source is observed.

- **<add>**may have more items**</add>**

The basic idea of fitting spectra parameters is to make the count cube generated by the model be as similar to the observation data as possible. The calculation process can be summarized as follows. First of all, we have to generate a spectral model for every source in the region of interest based on the Fermi database. The database includes LAT four-year Point Source Catalog (3FGL), Galactic diffuse emission (gll_iem_v06.fits) and isotropic emission (iso_P8R2_SOURCE_V6_v06.txt). Then we can produce a count cube based on the model. Generally speaking, the difference of the count cubes between the model and observation is obvious. Then, the Fermi software adjusts the parameters to make the difference smaller. Until the errors are acceptable, the software outputs the final fitted parameters.

We use a power-law-exponential-cutoff (PLExpCutoff) model to fit the observation data and it is a special case of power-law-super-exponential-cutoff (PLSuperExpCutoff) model. The spectrum of PLSuperExpCutoff can be described by the function:

$$\frac{dN}{dE} = N_0 \left(\frac{E}{E_0} \right)^{\gamma_1} exp \left(- \left(\frac{E}{E_c} \right)^{\gamma_2} \right) \tag{2.31}$$

where N_0 is prefactor, E_c is the cutoff energy and the E_0 is a scale parameter. PLExp-Cutoff model is the special case where $\gamma_2 = 1$. Our aim is to fit the parameters N_0, E_c and γ_1 to make the model be more consistent with observation data.

2.3.1 Correctness Verification of Data Processing

Before analyzing the observation of my target sources, it is reasonable to test if my procedure of data processing is right or not. In order to do so, I try to do analysis for 2 pulsars whose names are J0007+7303 and J0534+2200. The reason I choose these two pulsars is that in previous study, they are bright and easy to detect with a large TS value — the TS values are 43388 and 102653 for J0007+7303 and J0534+2200 respectively. The data is from *this paper*.

In the spectra fit process, I do not use the same fit parameters as the the paper, (for instance, the number of free parameters are different) however, I get the similar result as the table 2.1 showing. In this table, I use the observation data from 2009-01-01 to 2013-02-01 in order to try to be consistent with the paper. In addition, I also fit spectra with data end up to 2018-02-01 to test how much improvement the Fermi Pass 8 Lat data has over the previous version. The results of year 2018 data is showed in table 2.2.

The table 2.1 and table 2.2 mainly show 2 pieces of information. Firstly, my procedure of dealing with observation data has no big problems, so basically I can trust fit results of my target sources. Secondly, the Fermi Pass 8 Lat Data has improves the accuracy a lot. For example, as the table 2.1 showing, the photon indexes are 1.30 ± 0.02 and 1.4 ± 0.1,

	Test			Paper		
	Γ	E_c (MeV)	TS	Γ	E_c (MeV)	TS
J0007+7303	1.30 ± 0.02	2010 ± 85	96979	1.4 ± 0.1	4700 ± 200	43388
J0534+2200	2.07 ± 0.01	9880 ± 572	239015	1.9 ± 0.1	4200 ± 200	102653

Table 2.1: The Spectra Fit Result

	Γ	E_c (MeV)	TS
J0007+7303	1.34 ± 0.02	2204 ± 67	210166
J0534+2200	2.01 ± 0.01	9173 ± 372	449946

Table 2.2: Fit Results With Data From Year 2009 To Year 2018

which means that the errors reduce a lot. Additionally, the TS value is more than double as before.

2.3.2 PSR J0218+4232

Our ROI is a circle with radius of $20°$ and all parameters of sources which are $8°$ outside of the center are fixed. For sources within $8°$, their parameters are the same as the default values. In our case, there are 7 point sources which have free parameters. In the figure 2.6, the green circles represent those free sources while the purple circles represent fixed sources. We need to notice that in the outer parts of the count map, there are some of very bright sources which have no free parameters. The reasons is that the they are so far away from our target source that the Fermi telescope can distinguish if a photon comes from the target source or the outer sources. As a result, we do not need to fit any parameters for those outer sources. However, it is another case for the nearby sources.

Count Maps And Count Cubes

In the left of the figure 2.6 is the count map of PSR J0218+4232. In the center of the left figure, we can clearly see our target source. The dimension of the figures seems to be weird and the reason why we have 141 pixels for both x and y axis is that we select a circle region from the original data. However, when we generate a count map, we have to assign the sizes for x and y axis separately, which means that our a count map is actually rectangular. As a result, we have to crop a rectangular from the original circle region and in this case, we choose the rectangular as a square.

The figure 2.7 is a comparison of PSR J0218+4232's count maps in different energy bands. The count map in about 100MeV is so messy that we can hardly distinguish our target source while in about 30GeV so faint that there are no recorded photon around the
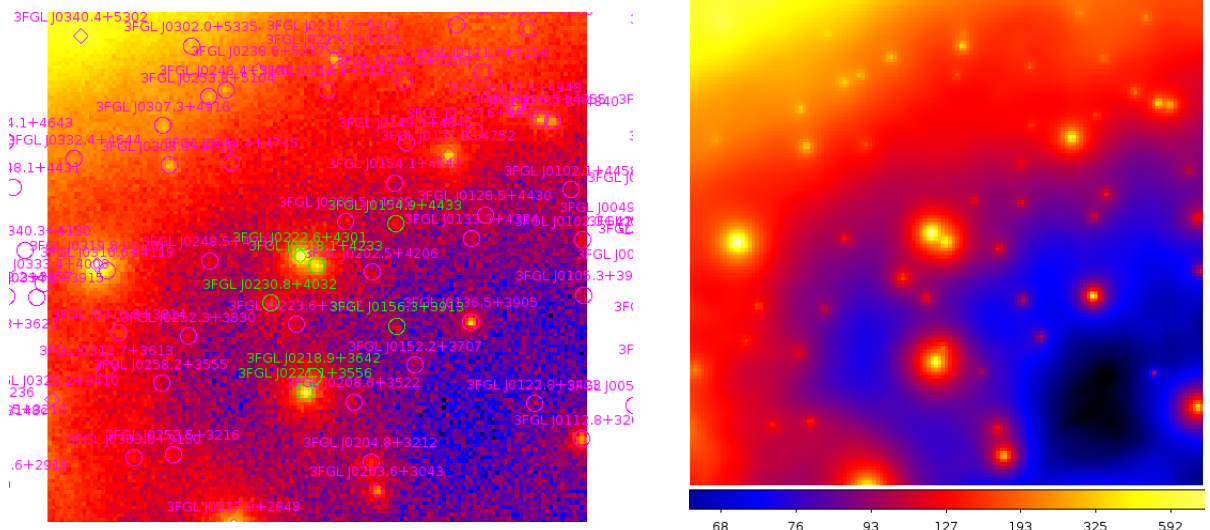
Figure 2.6: *The count map of PSR J0218 (left) and the count map generated by the model. In the left figure, the green circles are free sources while the purple circles are fixed sources. The size of the figure is 141 pixels × 141 pixels, and each pixel is 0.2° × 0.2°.*
<change>The figure color bar is a problem. I need to use some other tools to merge the two color bars.)</change>
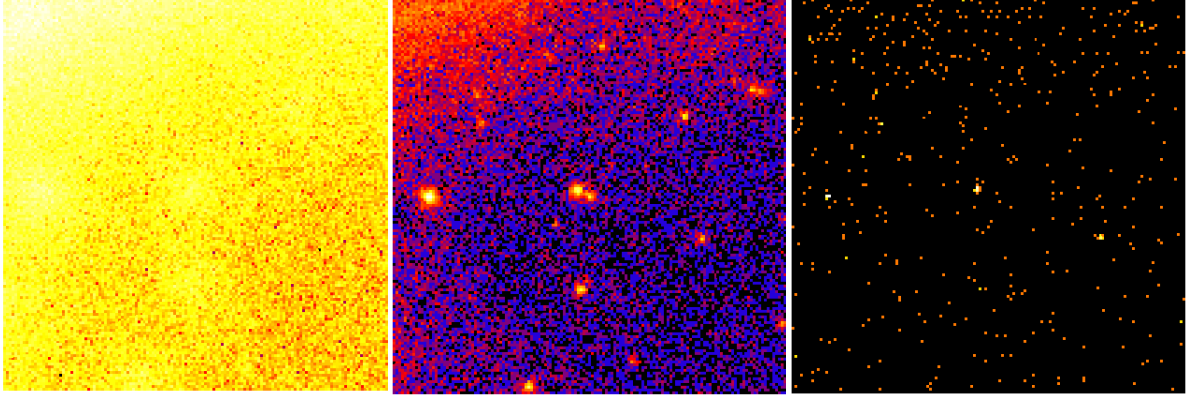
Figure 2.7: *Three figures of PSR J0218+4232's count cube. The energy range of the figure in the left: 100∼123MeV, middle: 1.873∼2.310GeV, right: 35.11∼43.29GeV.*
<add>add color bar</add>

source. We choose three circle regions whose centers are the our target sources and the radii are 1000 ″ for all of the three figures and then calculate the total photon counts of the selected regions. As the following table 2.3 shown, though total photon counts around our target source are similar between the left and middle map, the counts per energy is quite different. Therefore, we focus more on the middle energy parts (500MeV ∼ 50GeV). This means that when doing binned analysis, we divide more bins in the middle part.

Binned Likelihood Analysis

The figure 2.6 shows that the fit result of the model is similar to the observation. However, there are lots of small red pixels in the left figure (generated directly by the observation data) while the right figure is very "clean". This means that a lot of photon are thought as generated by the modeled source. Thus in our model, the sources are generally slightly brighter than the observation. However, our target source is an exception. In the region

	Left	Middle	Right
Total counts	78	93	0
Energy range (MeV)	100~123	1873~2310	35110~43290
Counts / MeV	3.39	0.213	0.000

Table 2.3: *Photon counts of count maps in different energy bands.*

we have used before (the center is the target source, and the radius is $1000''$), the total photon count in the left figure is 1815 compare to 1737 in the right figure.

The reason why the count map generated directly by the observation data is a lot more messy is that our modeled source is generated according to the Fermi database and their spatial position is fixed. This means that if a photon comes from a particular direction and there is no any known pulsar in that direction, this photon has to be classified to other directions in which there are other modeled pulsars. Thus, the spatial positions of photons are different between the observation and the model and the count maps generated directly from models are usually cleaner.
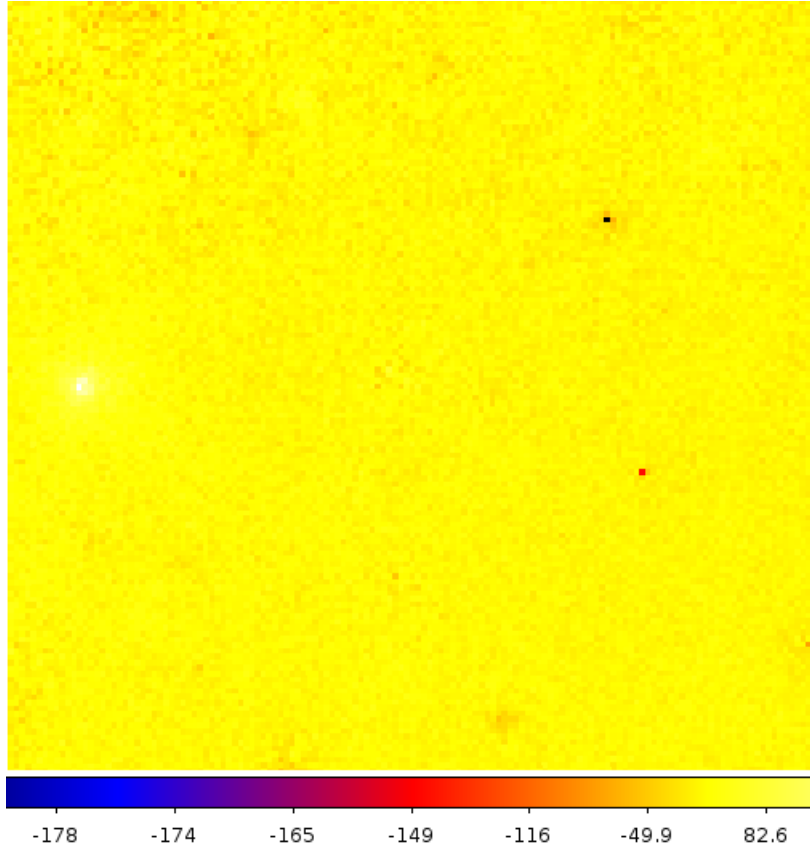
Figure 2.8: *The residual map shows the difference between the observation and the model. It is generated by subtracting the photon counts of each pixel between the count maps of observation and the model.* **<change>**ugly, scale may be wrong**</change>**

The figure 2.8 generally describes how well our model is compared to the observation

data. There are some black dots and bright dots in the residual map which means that the absolute photon counts between the model and the observation differ a lot. However, it is acceptable because the original value is much larger. The absolute values of most of other pixels are less than 10 implying that the global fit is fine.

	Value	Error
Prefactor (N_0)	1.71×10^{-11}	0.0610×10^{-12}
Index1 (γ_1)	1.8999	0.0395
Cutoff (E_c, MeV)	3794.25	396.447

Table 2.4: *Fit parameters of the model. The parameters are corresponding to the equation 2.31.* ***<add>****add comparison with previous data later.)****</add>*** ***<change>****the table is ugly****</change>***
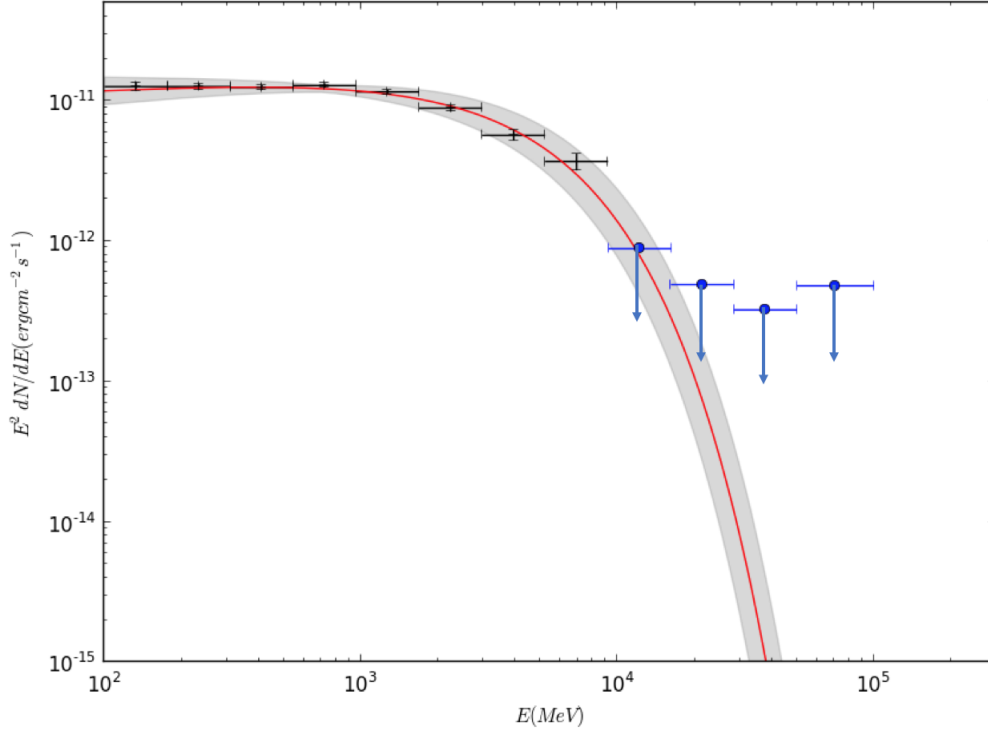

Figure 2.9: *The log-log plot of flux to energy. The grey shade represents fitting errors, black points with error bars are flux points, the blue dots are upper values and the red line is the PLExpCutoff model multiplied by E^2. Flux points are fitted separately by dividing the total energy bin (100 MeV $\sim$ 100 GeV) into multiple energy bins. The horizontal error bars represents the width of each bin.*
(The figure should use legends, but for now I have problem setting those styles, may be my matplotlib version is too old.)
<change>*legends, arrows****</change>***

The table 2.4 lists the results of fitting parameters. The figure 2.9 plot the spectrum according to the function 2.31. One thing should be noticed is that we need to multiply E^2 to the function 2.31 to get the flux. The figure 2.9 shows that the global fit is consistent with flux points fitted by each energy bin separately. The TS value for the fit is 7110, which gives us a significance level $\sigma \approx \sqrt{TS} = 84$. This strongly implies the presence of

our target source. We can also use a TS map to test the presence of the source as the figure 2.15 showing.
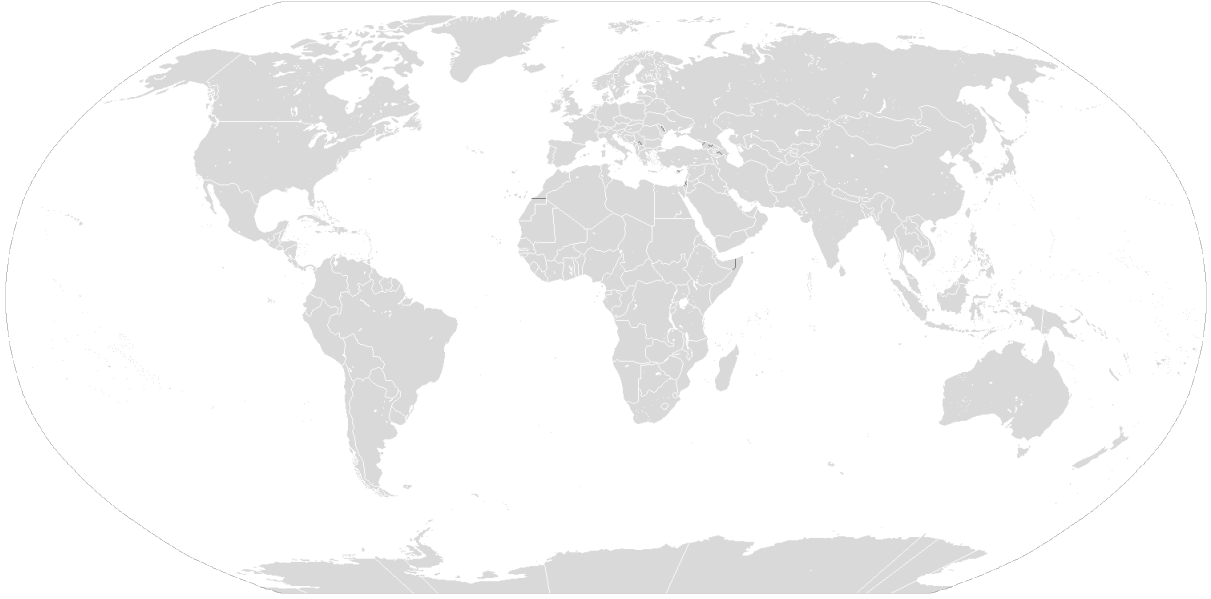
Figure 2.10: *<change>The figure should be a TS map, but the new TS map has not been generated yet. The previous TS map does not use the best fit parameters, so I have to re-generate the TS map. And this world map is just a reminder and it may be used a lot.</change>*

2.3.3 PSR J1824.6-2452

The ROI region is a circle whose radius is 20° and all sources outside of 8° are fixed. There are 6 free sources in the region of 8°. The figure 2.11 is a combination of count maps of observation data and the model.

Count Maps And Count Cubes

As the figure 2.11 shown, the PSR J1824.6 is much dimmer than PSR J0218+4232, which implies that the fitting result may be worse. In general, the two figures are quite similar, except that the modeled count map lacks some details and the reason was explained in the previous section 2.3.2.

The figures 2.12 are count maps of PSR J1824.6-2452 in different energy bands. The target pulsar is too faint in very high energy band and interfered too much by the ambient environment in low energy band (around 100MeV). Because our target source is near the M28 globular cluster and very faint, it is reasonable that the fitting result is worse than PSR J0218+4232.

Binned Likelihood Analysis

The differences of the count map between the observation data and the model are described as the figure 2.13.
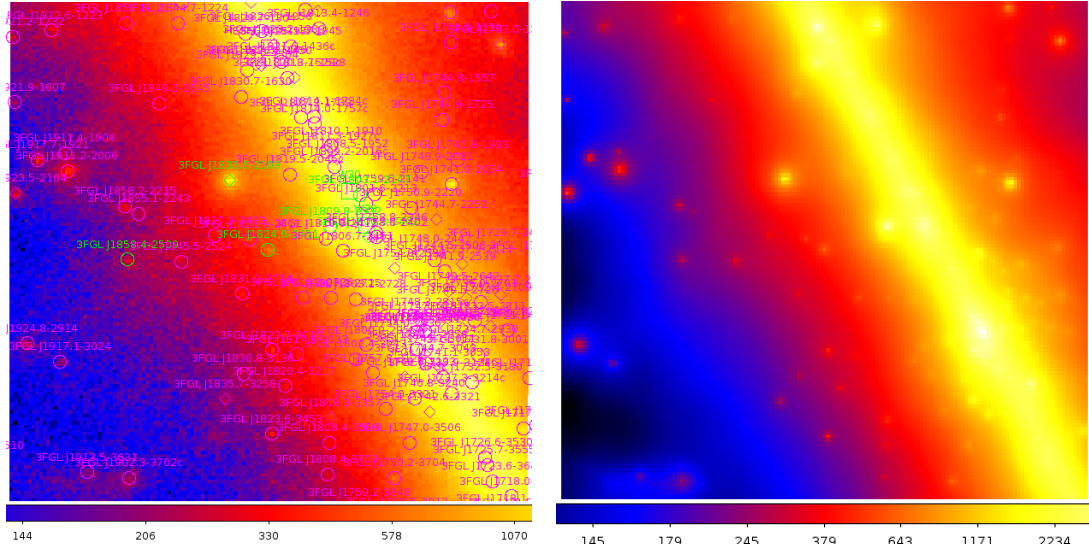
Figure 2.11: *The count map of PSR J1821.6 (left) and the count map generated by the model. In the left figure, the green circles are free sources while the purple circles are fixed sources. The sizes of the both figures are 141 pixels × 141 pixels, and each pixel is 0.2° × 0.2°.*
(The figure color bar is a problem. I need to use some other tools to merge the two color bars. Also, I think I should make the color bar be vertical instead of horizontal.)
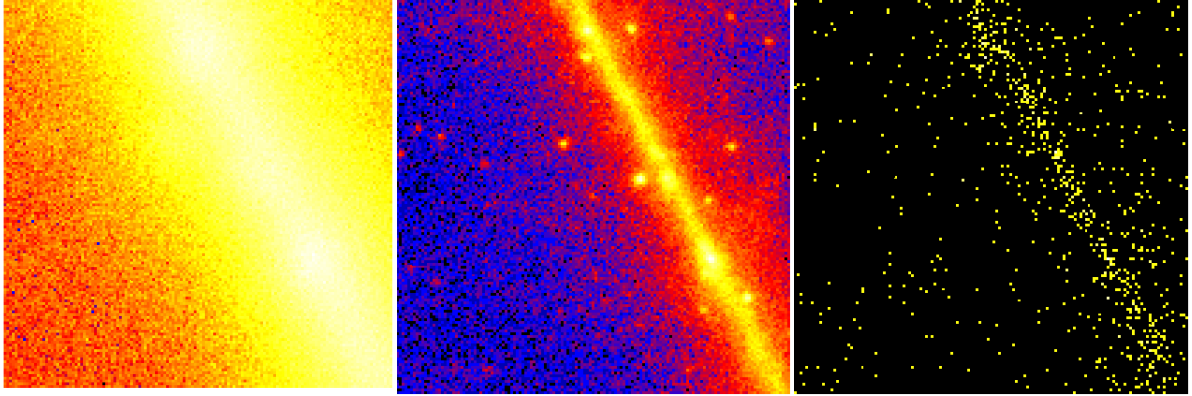

Figure 2.12: *Three figures of PSR J1824.6's count cube. The energy range of the figure in the left: 100∼123MeV, middle: 1.873∼2.310GeV, right: 81.11∼100GeV.*
*<**add**>add color bar</**add**>*

There is an obvious black dot in the figure 2.13 and the value of the dot is large — 1299. The original value from the observation data is 4503. I think the model is acceptable because the source in this pixel is fixed and far away from our target source (<**question**>I'm not sure yet.</**question**>). So the value of this source does not contribute too much to the center. The values of most other pixels are below 20 implying that the global fit result is acceptable.

The figure 2.14 shows that the global fit is consistent with the flux points generated by fitting sub-energy bins. However, we should notice the first flux points which is denoted as a blue square in the figure 2.14. This flux points is significantly smaller than the global fit (the red line in the figure). What's more, the upper value for the first energy bin is still slightly smaller. <**question**>I think it is because that the flux points are fitted separately and are independent to the global fit. In fact, we use a single power-lay model to fit each sub-energy bin while PLExpCutoff model to do the global fit. As we have
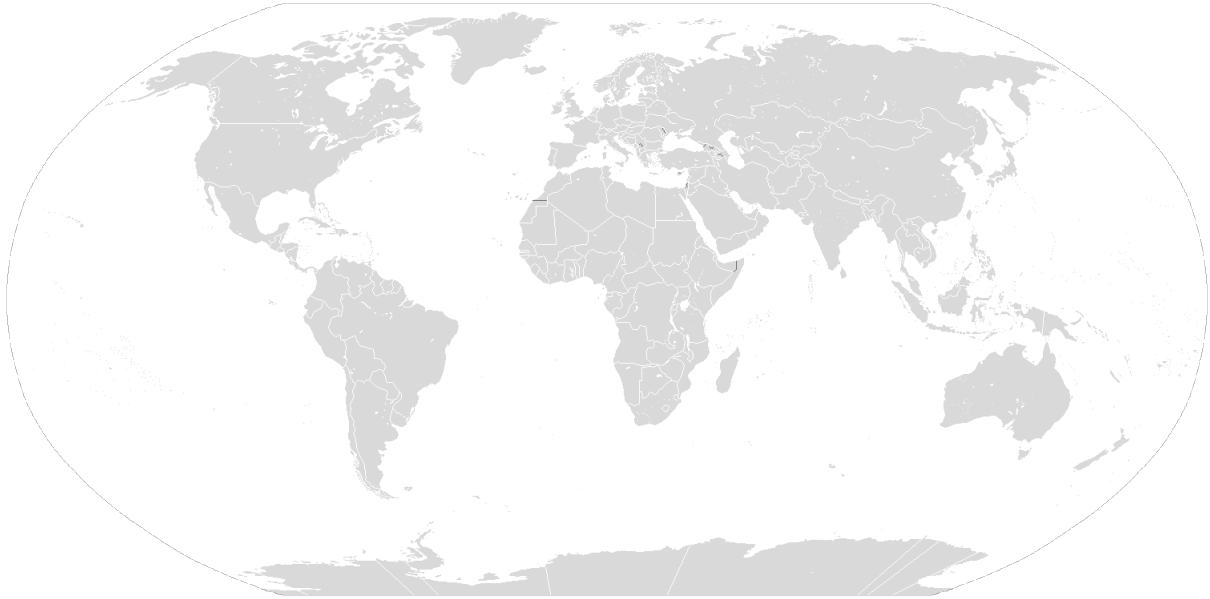
23
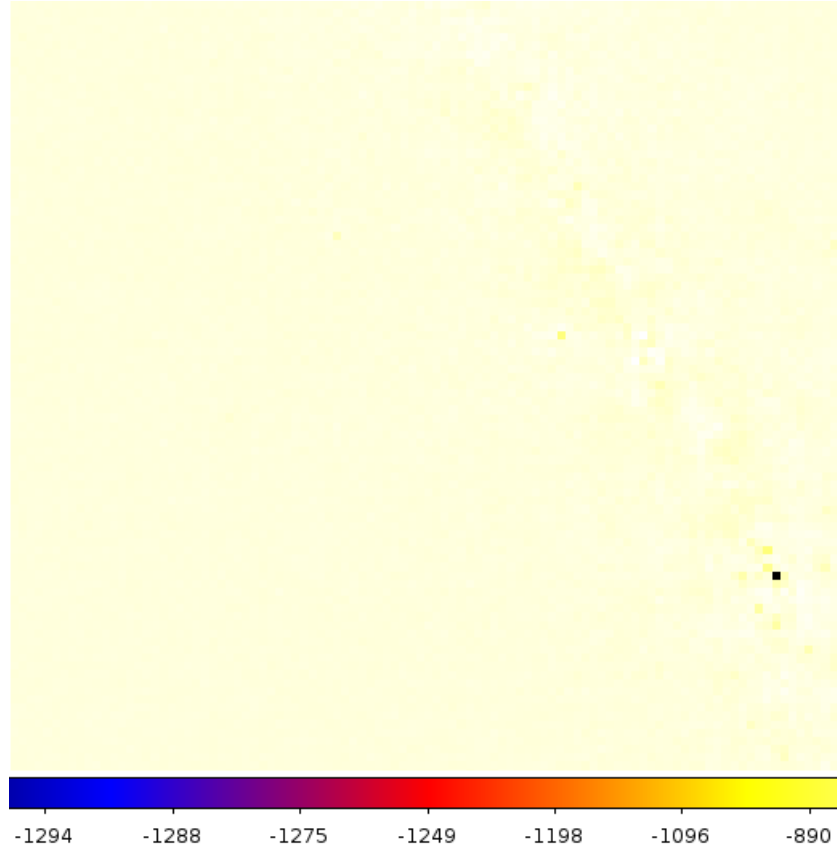
Figure 2.13: *The residual map shows the difference in photon counts between the observation and the model* <change>*ugly*</change>
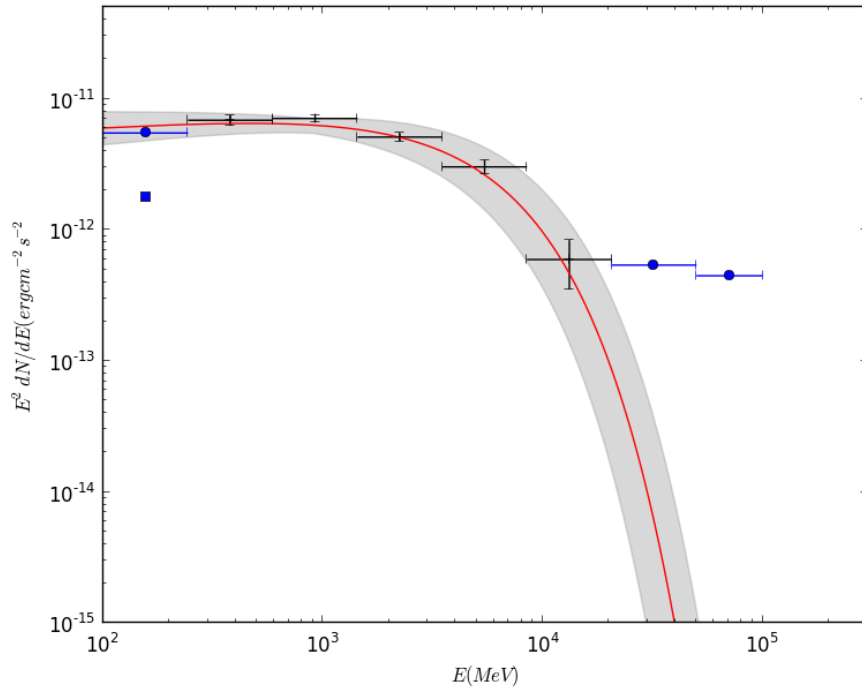
Figure 2.14: *The log-log plot of flux to energy.* <change>*should use legends, add arrows for upper values, make the label fonts larger.*</change>

explained previously, the lower energy part of the observation (around 100 MeV) is not reliable. As a result, the separate fit for the first energy bin is not as reliable as the global

fit and it is reasonable that the two fitting results are not consistent. When this happens, we have more confidence on the global fit than the separate fit.</**question**>

Figure 2.15: *<**change**>The figure should be a TS map, but the new TS map has not been generated yet. The previous TS map does not use the best fit parameters, so I have to re-generate the TS map. And this world map is just a reminder and it may be used a lot.</**change**>*

2.3.4 PSR J1939+2134

<**add**>continue here</**add**>